

Studies of granularity of a hadronic calorimeter for tens-of-TeV jets at a 100 TeV pp collider

C.-H. Yeh^a, S.V. Chekanov^b, A.V. Kotwal^{c,d}, J. Proudfoot^b, S. Sen^c, N.V. Tran^d, S.-S. Yu^a

^a *Department of Physics, National Central University, Chung-Li, Taoyuan City 32001, Taiwan*

^b *HEP Division, Argonne National Laboratory, 9700 S. Cass Avenue, Argonne, IL 60439, USA.*

^c *Department of Physics, Duke University, USA*

^d *Fermi National Accelerator Laboratory*

^e *Department of Physics, Michigan State University, 220 Trowbridge Road, East Lansing, MI 48824*

Abstract

Jet substructure variables for hadronic jets with transverse momenta in the range from 2.5 TeV to 20 TeV were studied using several designs for spacial size of calorimeter cells. The studies used the full Geant4 simulation of calorimeter response combined with realistic reconstruction of calorimeter clusters used in jet reconstruction. In most cases considered in this study the results indicate that the performance of jet-substructure reconstruction improves with reducing cell sizes from 20 cm x 20 cm to 5 cm x 5 cm.

Keywords: multi-TeV physics, pp collider, future hadron colliders, FCC, SppC

1. Introduction

Particle collisions at energies beyond those attained at the LHC will lead to many challenges for detector technologies. Future experiments, such as high-energy LHC (HE-LHC), future circular pp colliders of the European initiative, FCC-hh [1] and the Chinese initiative, SppC [2] will be required to measure high-momentum bosons (W , Z , H) and top quarks with strongly collimated decay products that form jets. Studies of jet substructure can help identify such particles.

The reconstruction of jet substructure variables for collimated jets with transverse momentum above 10 TeV require an appropriate detector design. The most important for reconstruction of such jets are tracking and calorimeter. Recently, a number of studies [3, 4, 5] have been discussed using various fast simulation tools, such as Delphes [6], in which momenta of particles are smeared to mimic detector response.

A major step towards the usage of full Geant4 simulation to verify the granularity requirements for calorimeters was made in [7]. The studies included in this paper have illustrated a significant impact of granularity of electromagnetic (ECAL) and hadronic (HCAL) calorimeters on the shape of hadronic showers calculated using calorimeter

Email addresses: jwzuzelski18@gmail.com (C.-H. Yeh), chekanov@anl.gov (S.V. Chekanov), ashutosh.kotwal@duke.edu (A.V. Kotwal), proudfoot@anl.gov (J. Proudfoot), sourav.sen@duke.edu (S. Sen), ntran@fnal.gov (N.V. Tran), syu@cern.ch (S.-S. Yu)

hits for two particles separated by some angle. It was concluded that high granularity is essential in resolving two close-by particles for energies above 100 GeV.

This paper makes another step in understanding of this problem in terms of high-level physics quantities typically used in physics analyses. Similar to the studies presented in [7], this paper is based on a full Geant4 simulation with realistic jet reconstruction.

2. Simulation of detector response and event reconstruction

The description of the detector and software used for this study is discussed in [7]. We use the SiFCC detector geometry with a software package that represents a versatile environment for simulations of detector performance, testing new technology options, event reconstruction techniques for future 100 TeV colliders.

The GEANT4 (version 10.3) [8] simulation of calorimeter response was complemented with the full reconstruction of calorimeter clusters formed by the Pandora algorithm [9, 10]. Calorimeter clusters were built from calorimeter hits in the ECAL and HCAL after applying the corresponding sampling fractions. No other corrections are applied. Hadronic jets were reconstructed with the FASTJET package [11] using the anti- k_T algorithm [12] with a distance parameter of 0.5.

In the following discussion, we use the simulations of a heavy Z' boson, a hypothetical gauge boson that arises from extensions of the electroweak symmetry of the Standard Model. The Z' bosons were simulated with the masses, $M = 5, 10, 20$ and 40 TeV. The lowest value represents a typical mass that is within the reach of the LHC experiments. The value 40 TeV represents the physics reach for a 100 TeV collider. The Z' particles are forced to decay to two light-flavor jets ($q\bar{q}$), W^+W^- or $t\bar{t}$, where W and t decay hadronically. In all such scenarios, two highly boosted jets are produced, which are typically back-to-back in the laboratory frame. Typical transverse momenta of such jets are $\simeq M/2$. The main difference between considered decay types lays in different jet substructure. In the case of the $q\bar{q}$ decays, jets do not have any internal structure. In the case of W^+W^- , each jet originates from W , thus it has two subjects because of the decay $W \rightarrow q\bar{q}$. In the case of hadronic top decays, jets have three subjects due to the decay $t \rightarrow W^+b \rightarrow q\bar{q}b$. The signal events were generated using the PYTHIA8 generator with the default settings, ignoring interference with SM processes. The event samples used in this paper are available from the HepSim database [13].

3. Studies of jet properties

First let us consider several variables that represent jet substructure using different types of calorimeter granularity. The question we want to answer is how close the reconstructed jet substructure variables reflect the input “truth” values that are reconstructed using input particles directly from the PYTHIA8 generator.

In this study we use the jet effective radius and jet splitting scales as benchmark variables to study jet substructure properties for different calorimeter granularity scenarios. The effective radius is the average of the energy weighted radial distance in $\eta-\phi$ space of jet constituents. Recently, it has been studied for multi-TeV jets in Ref.[14]. A jet k_T splitting scale [15] is defined as a distance measure used to form jets by the

59 k_T recombination algorithm [16, 17]. This variable has been studied by ATLAS [18],
60 and more recently in the context of 100 TeV physics [14]. The splitting scale is defined
61 as $\sqrt{d_{12}} = \min(p_T^1, p_T^2) \times \delta R_{12}$ [18] at the final stage of the k_T clustering, where two
62 subjets are merged into the final one.

63 Figures 1 and 2 show the distributions of the jet effective radius and jet splitting
64 scale for different jet transverse momenta and HCAL granularities. The reconstructed-
65 level distributions significantly disagree with the distributions reconstructed using truth-
66 level particles. The distribution reconstructed with the cell sizes 1 cm×1 cm are clos-
67 est to the truth-level variables. The distributions reconstructed using the cell size of
68 20 cm×20 cm, which is similar to the nuclear interaction length of Fe ($\lambda_I \simeq 17$ cm) the
69 SiFCC calorimeter [7], show the largest discrepancy with the truth-level variables. Note
70 that, in terms of closeness of reconstructed distributions to the truth level, there is no
71 significant difference between 5 cm×5 cm, 2 cm×2 cm and 1 cm×1 cm choices. Both
72 the ATLAS and CMS detectors use cell sizes which are close to the nuclear interaction
73 length of the HCAL cells.

74 4. Study of detector performance with soft drop mass

75 In this section, we use the jet mass computed with a specific algorithm, soft drop
76 declustering, to study the performance of detector with various detector cell sizes and
77 center-of-mass (c.m.) energies.

78 4.1. The technique of soft drop declustering

79 The soft drop declustering [19] is a grooming method that removes soft wide-
80 angle radiation from a jet. The constituents of a jet j_0 are first reclustered using
81 the Cambridge-Aachen (C/A) algorithm [20, 21]. Then, the jet j_0 is broken into two
82 subjets j_1 and j_2 by undoing the last stage of C/A clustering. If the subjets pass
83 the following soft drop condition, jet j_0 is the final soft-drop jet. Otherwise, the algo-
84 rithm redefines j_0 to be the subjet with larger p_T (among j_1 and j_2) and iterates the
85 procedure.

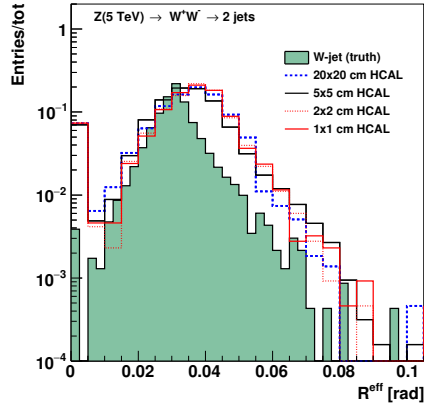
$$\frac{\min(p_{T1}, p_{T2})}{p_{T1} + p_{T2}} > z_{\text{cut}} \left(\frac{\Delta R_{12}}{R_0} \right)^\beta, \quad (1)$$

86 where p_{T1} and p_{T2} are the transverse momenta of the two subjets, z_{cut} is soft drop
87 threshold, ΔR_{12} is the distance between the two subjets in the rapidity-azimuth angle
88 plane (y - ϕ), R_0 is the characteristic radius of the original jet, and β is the angular
89 exponent.

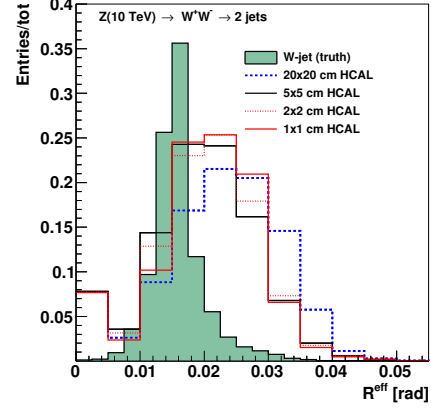
90 In our study, we compare the performance of future detector when setting $\beta = 0$
91 versus when setting $\beta = 2$. For $\beta = 0$, the soft drop condition depends only on the z_{cut} .
92 For $\beta = 2$, the condition depends on the angular distance between the two subjets and
93 z_{cut} and the algorithm becomes infrared and collinear safe.

94 4.2. Analysis method

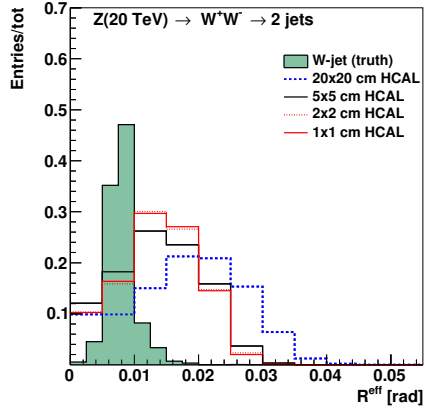
95 We employ the following method to quantify the detector performance and find out
96 the cell size that gives the best separation power to distinguish signal from background.
97 For each configuration of detector and c.m. energy, we draw the receiver operating
98 characteristic (ROC) curves in which the x-axis is the signal efficiency (ϵ_{sig}) and y-axis



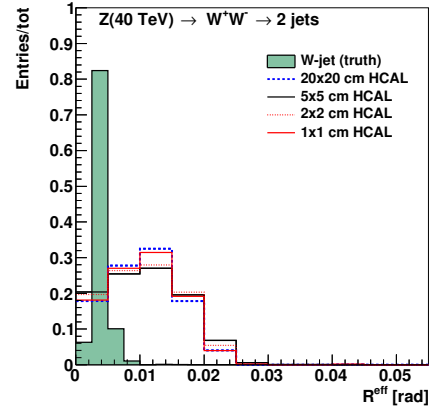
(a) 5 TeV



(b) 10 TeV

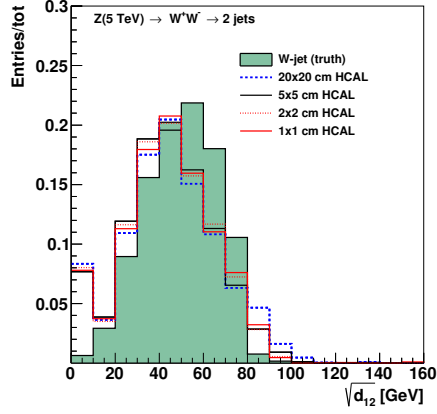


(c) 20 TeV

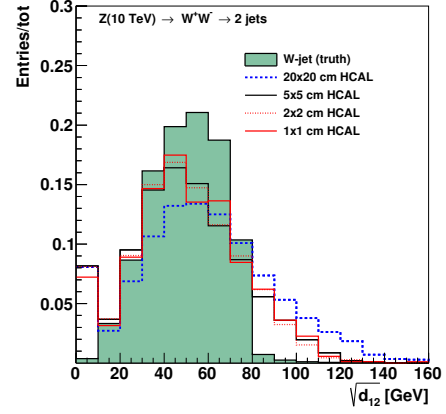


(d) 40 TeV

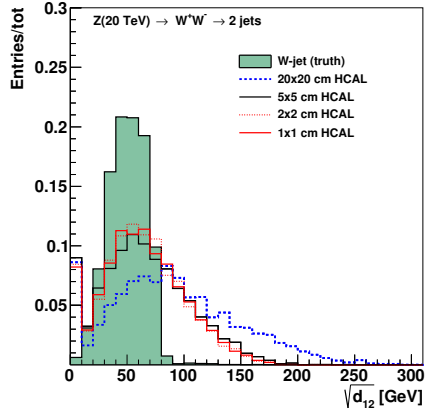
Figure 1: Jet effective radius for different jet transverse momenta and HCAL granularities.



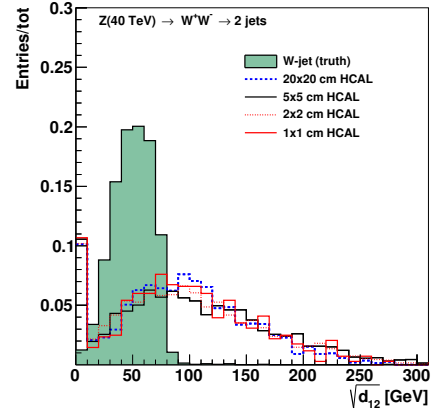
(a) 5 TeV



(b) 10 TeV



(c) 20 TeV



(d) 40 TeV

Figure 2: Jet splitting scale for different jet transverse momenta and HCAL granularity.

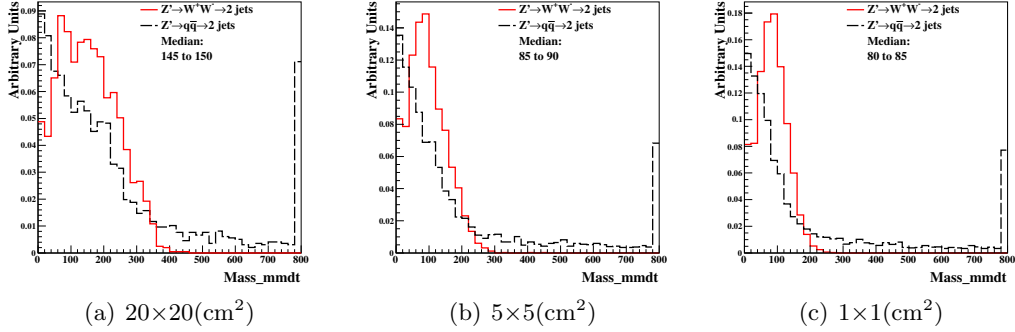


Figure 3: Distributions of soft drop mass for $\beta=0$, with 20 TeV c.m. energies and three different detector cell sizes: 20×20 , 5×5 , and 1×1 (cm^2). The signal (background) process is $Z' \rightarrow WW$ ($Z' \rightarrow q\bar{q}$).

is the inverse of background efficiency ($1/\epsilon_{\text{bkg}}$). In order to scan the efficiencies of soft drop mass cuts, we vary the mass window as follows. We first look for the median bin i_{med} ¹ of the soft drop mass histogram from simulated signal events. Taking the right boundary of bin i_{med} as the center of mass window x_{center} , we start increasing the width of mass window symmetrically on the left and on the right of x_{center} , in steps of 5 GeV, i.e. the narrowest mass window is $[x_{\text{center}} - 5, x_{\text{center}} + 5]$. If one side reaches the boundary of the mass histogram, we only increase the width on the other side, also in steps of 5 GeV. For each mass window, there will be corresponding ϵ_{sig} and ϵ_{bkg} , which gives a point in the ROC curves.

4.3. Results and conclusion

Figures 3, 5, 7, and 9 show a few representative distributions for the soft drop mass for $\beta = 0$ and $\beta = 2$ with different c.m. energies and detector cell sizes; the signals considered are $Z' \rightarrow WW$ and $Z' \rightarrow t\bar{t}$.

Figures 4, 6, 8, and 10 show the ROC curves for different detector cell sizes and c.m. energies.

These studies show that the reconstruction of soft drop mass improves with decrease of the HCAL cell sizes. Figures 4 and 6 show that for $\beta = 0$ the smallest detector cell size, $1 \text{ cm} \times 1 \text{ cm}$, has the best separation power at $\sqrt{s}=5, 10$, and 20 TeV when the signal is $Z' \rightarrow WW$ and at $\sqrt{s}=10$ and 20 TeV when the signal is $Z' \rightarrow t\bar{t}$. On the contrary, Figs. 8 and 10 show that for $\beta = 2$ the smallest detector cell size does not have improvements in the separation power with respect to those with larger cell sizes. In fact, the performances of the three cell sizes are similar. In addition, sometimes bigger detector cell sizes, $5 \text{ cm} \times 5 \text{ cm}$ or $20 \text{ cm} \times 20 \text{ cm}$ have the best separation power.

We also find that the soft drop mass with $\beta = 0$ has better performance for distinguishing signal from background than for $\beta = 2$. Therefore, we will apply requirements on this variable when studying the other jet substructure variables.

¹The integral from bin 0 to bin i_{med} ($i_{\text{med}} - 1$) should be greater (less) than half of the total number of events. Note, the bin width is 5 GeV.

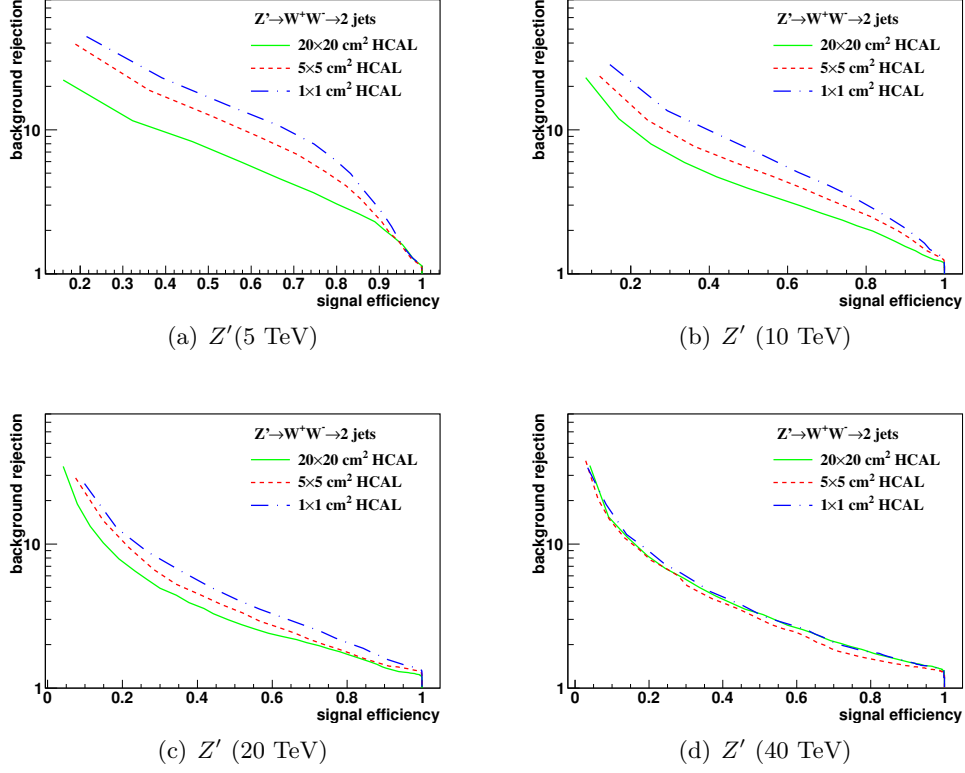


Figure 4: The ROC curves of soft drop mass selection for $\beta=0$ with 5, 10, 20, 40 TeV c.m. energies. Three different detector cell sizes are compared: 20×20 , 5×5 , and $1 \times 1 \text{ (cm}^2\text{)}$. The signal (background) process is $Z' \rightarrow WW$ ($Z' \rightarrow q\bar{q}$).

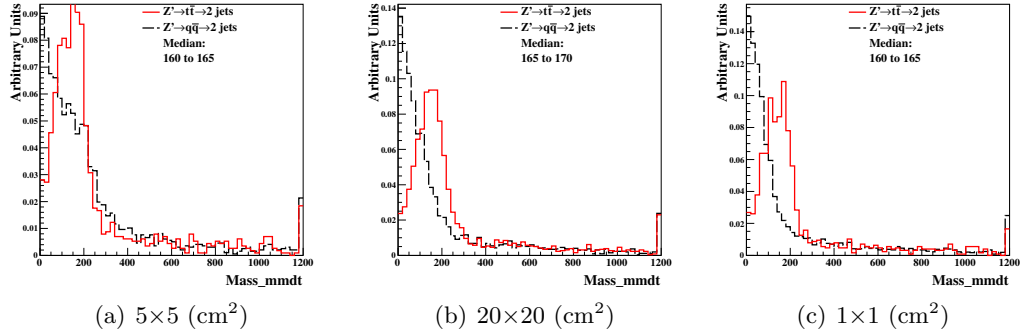


Figure 5: Distributions of soft drop mass for $\beta=0$, with 20 TeV c.m. energies and three different detector cell sizes: 20×20 , 5×5 , and $1 \times 1 \text{ (cm}^2\text{)}$. The signal (background) process is $Z' \rightarrow t\bar{t}$ ($Z' \rightarrow q\bar{q}$).

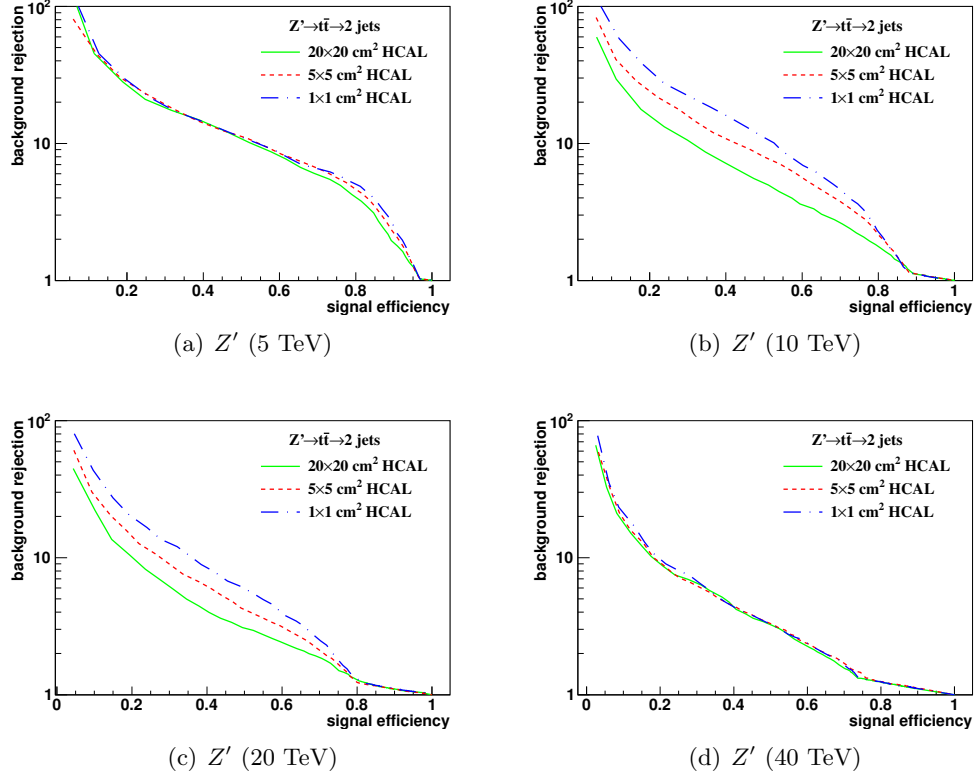


Figure 6: The ROC curves of soft drop mass selection for $\beta=0$ with 5,10, 20, 40 TeV c.m. energies. Three different detector cell sizes are compared: 20×20 , 5×5 , and 1×1 (cm^2). The signal (background) process is $Z' \rightarrow t\bar{t}$ ($Z' \rightarrow q\bar{q}$).

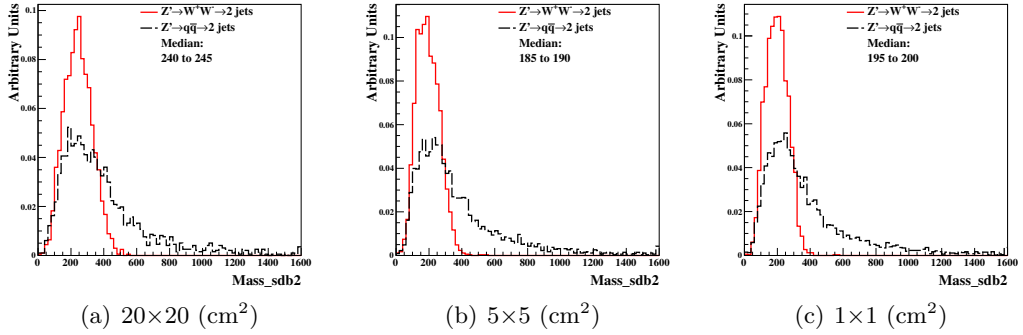


Figure 7: Distributions of soft drop mass for $\beta=2$, with 20 TeV c.m. energies and three different detector cell sizes: 20×20 , 5×5 , and 1×1 (cm^2). The signal (background) process is $Z' \rightarrow WW$ ($Z' \rightarrow q\bar{q}$).

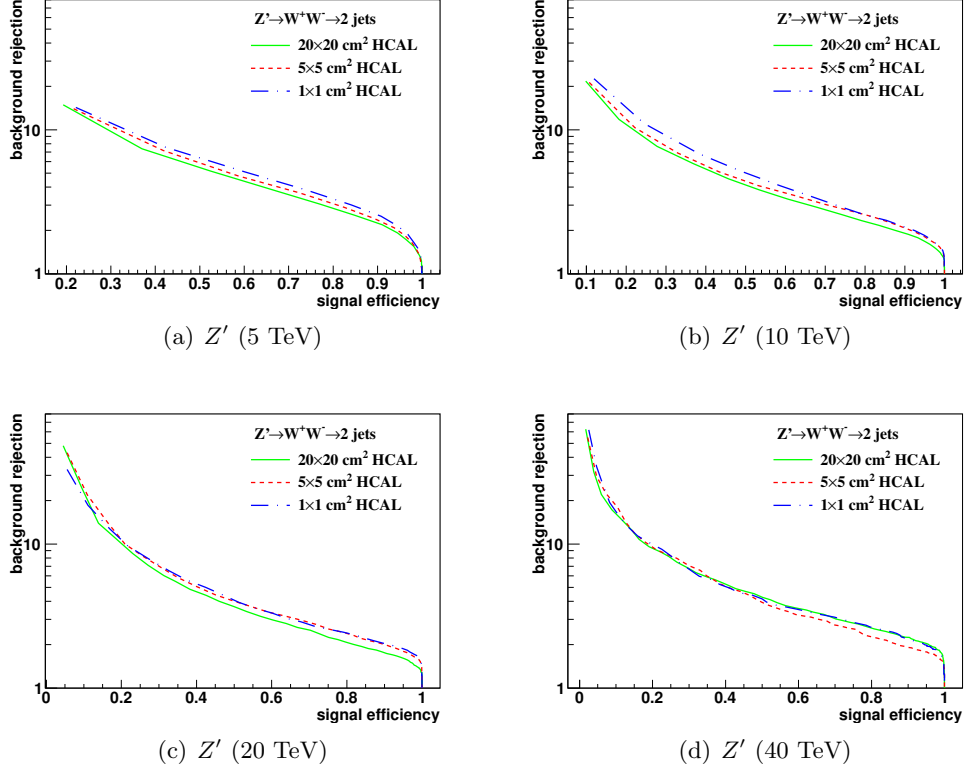


Figure 8: The ROC curves of soft drop mass selection for $\beta=2$ with 5, 10, 20, 40 TeV c.m. energies. Three different detector cell sizes are compared: 20×20 , 5×5 , and $1 \times 1 \text{ (cm}^2\text{)}$. The signal (background) process is $Z' \rightarrow WW$ ($Z' \rightarrow q\bar{q}$).

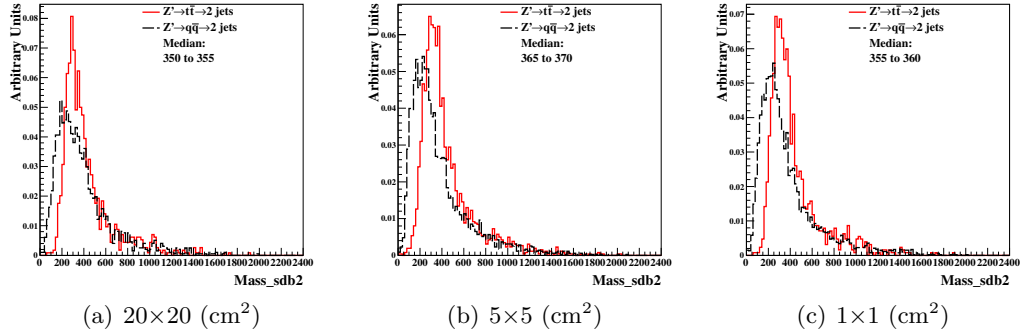
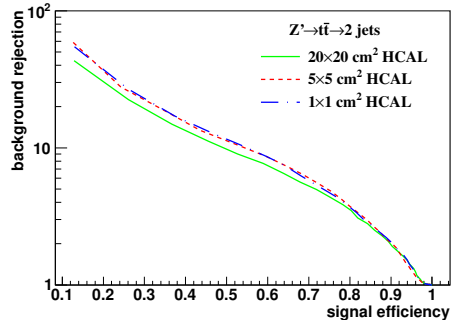
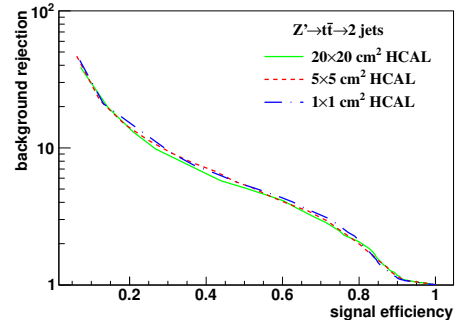


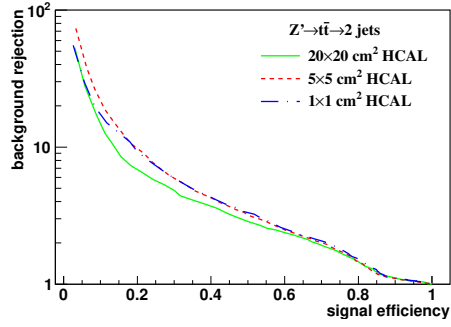
Figure 9: Distributions of soft drop mass for $\beta=2$, with 20 TeV c.m. energies and three different detector cell sizes: 20×20 , 5×5 , and $1 \times 1 \text{ (cm}^2\text{)}$. The signal (background) process is $Z' \rightarrow t\bar{t}$ ($Z' \rightarrow q\bar{q}$).



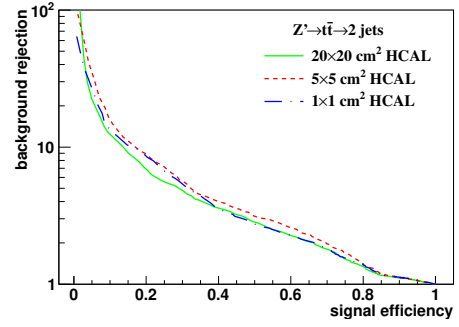
(a) $Z' (5 \text{ TeV})$



(b) $Z' (10 \text{ TeV})$



(c) $Z' (20 \text{ TeV})$



(d) $Z' (40 \text{ TeV})$

Figure 10: The ROC curves of soft drop mass selection for $\beta=2$ with 5, 10, 20, 40 TeV c.m. energies. Three different detector cell sizes are compared: 20×20 , 5×5 , and 1×1 (cm^2). The signal (background) process is $Z' \rightarrow t\bar{t}$ ($Z' \rightarrow q\bar{q}$).

125 5. Study of detector performance with jet substructure variables

126 In this section, we use several jet substructure variables to study the performance
127 of detector with various detector cell sizes and c.m. energies.

128 5.1. N -subjettiness

129 The variable N -subjettiness [22], denoted by τ_N , is designed to “count” the number
130 of subjet(s) in a large radius jet so to separate signal jets from decays of heavy bosons
131 and background jets from QCD processes. The τ_N is the p_T -weighted angular distance
132 between each jet constituent and the closest subjet axis:

$$\tau_N = \frac{1}{d_0} \sum_k p_{T,k} \min\{\Delta R_{1,k}, \Delta R_{2,k}, \dots, \Delta R_{N,k}\}, \quad (2)$$

133 with a normalization factor d_0 :

$$d_0 = \sum_k p_{T,k} R_0.$$

134 The k runs over all constituent particles in a given large radius jet, $p_{T,k}$ is the transverse
135 momentum of each individual constituent particle, $\Delta R_{j,k} = \sqrt{(\Delta y)^2 + (\Delta \phi)^2}$ is the
136 distance between the constituent particle k and the candidate subjet axis j in the $y - \phi$
137 plane. The R_0 is the characteristic jet radius used in the anti- k_t jet algorithm.

138 In this analysis, the anti- k_t algorithm with $R = 0.4$ (AK4) is first employed to re-
139 construct jets. The subjet axes are obtained by running the exclusive k_t algorithm [23]
140 and reversing the last N clustering steps. Namely, when τ_N is computed, the k_t al-
141 gorithm is forced to return exactly N jets. If a large radius jet has N subjet(s), its
142 τ_N is smaller than τ_{N-1} . Therefore, in our analysis, the ratio of the τ_N variables, τ_{21}
143 (τ_2/τ_1) and τ_{32} (τ_3/τ_2), are used to distinguish the one-prong background jets and the
144 two-prong jets from W or the three-prong jets from top.

145 We use the ROC curves as described in Section 4.2 to analyze the detector perfor-
146 mance and determine the cell size that gives the best separation power to distinguish
147 signal from background. Following the suggestion by Ref. [24], requirement on the soft
148 drop mass with $\beta = 0$ is applied before the study of N -subjettiness. For each detector
149 configuration and c.m. energy, the soft drop mass selection is determined as follows.
150 First, we look for the median bin of the soft drop mass histogram from simulated signal
151 events as described in Section 4.2. Then, we compare the numbers of events in the
152 bins adjacent to the medium bin (bin $i_{\text{med}} - 1$ and bin $i_{\text{med}} + 1$). The bin with larger
153 number of events is added, in addition to the medium bin, to extend the mass window.
154 The procedure is repeated until the window contains at least 75% of the total number
155 of signal events.

156 In order to obtain the signal and background efficiencies, various ranges of the τ_{21}
157 and τ_{32} are scanned. Since some of the background distributions have long tails and
158 leak into the signal-dominated region, we use the following method as suggested by the
159 Pearson Lemma Method to determine the ranges of τ variables. First, we take the ratio
160 of the signal to background τ_{21} (τ_{32}) histograms. The boundaries of the bin (seed bin)
161 with maximum signal to background ratio (S/N) give us the first range of τ selection:

162 $x_{\text{low}}^{\text{seedbin}} < \tau_{21} < x_{\text{high}}^{\text{seedbin}}$. Then, we compare the S/N in the bins adjacent to the seed
 163 bin. The bin with larger S/N is added, in addition to the seed bin, to extend the τ_{21}
 164 selection window. Every window has its corresponding ϵ_{sig} and $1/\epsilon_{\text{bkg}}$ and an ROC
 165 curve is mapped out.

166 In addition to the ROC curves, we use the so-called "Mann-Whitney" test to quan-
 167 tify the detector performance. The value of Mann-Whitney is related to the integrated
 168 area under the ROC curve: if the value is bigger, it indicates the signal and background
 169 distributions have similar shapes and can not be well separated from each other. Vice
 170 versa, if the value is smaller, we can achieve a better signal and background separation.

171 Figures 11 and 13 show the distributions of τ_{21} and τ_{32} for $\sqrt{s} = 20$ TeV after
 172 applying requirement on the soft drop mass. The signals considered are $Z' \rightarrow WW$ (τ_{21})
 173 and $Z' \rightarrow t\bar{t}$ (τ_{32}). Figures 12 and 14 present the ROC curves from different detector
 174 cell sizes and c.m. energies, respectively. The smallest detector cell size (1×1 cm²)
 175 does not have the best separation power. In fact, in some cases, the best separation
 176 power comes from detector with bigger cell sizes (5×5 cm² and 20×20 cm²).

177 Figures 17 (a) and (b) present the summary plots of τ_{21} and τ_{32} with various detector
 178 cell sizes and c.m. energies using Mann Whitney U test. For τ_{21} at smaller c.m.
 179 energies, when cell size is smaller, the detector performance improves. However, when
 180 c.m. energy increases, no improvement is observed using the smallest detector cell size
 181 (1×1 cm²). For τ_{32} , the case is similar to τ_{21} . Even worse, with some c.m. energies,
 182 the bigger detector cell sizes (5×5 cm² and 20×20 cm²) have better separation power
 183 than the smallest detector size.

184 5.2. Energy correlation function

185 The energy correlation function (ECF) [25] is defined as follows:

$$ECF(N, \beta) = \sum_{i_1 < i_2 < \dots < i_N \in J} \left(\prod_{a=1}^N p_{Tia} \right) \left(\prod_{b=1}^{N-1} \prod_{c=b+1}^N R_{i_b i_c} \right)^\beta, \quad (3)$$

186 where the sum is looped all particles in the jet J , p_T is the transverse momentum of
 187 each individual particle, and R is the distance between two particles in the y - ϕ plane.
 188 In order to use a dimensionless variable, a parameter r_N is defined:

$$r_N^{(\beta)} \equiv \frac{ECF(N+1, \beta)}{ECF(N, \beta)}. \quad (4)$$

189 The idea of r_N comes from N-subjettiness τ_N . Both r_N and τ_N are linear in the
 190 energy of the soft radiation for a system of N partons with soft radiation. In gen-
 191 eral, if the system has N subjets, $ECF(N+1, \beta)$ should be significantly smaller than
 192 $ECF(N, \beta)$. Therefore, we can use this feature to distinguish jets with different num-
 193 ber of subjets. As in Section 5.1, the ratio r_N/r_{N-1} , denoted by C_N , (double ratios of
 194 ECFs) is used to study the detector performance:

$$C_N^{(\beta)} \equiv \frac{r_N^{(\beta)}}{r_{N-1}^{(\beta)}} = \frac{ECF(N-1, \beta) ECF(N+1, \beta)}{ECF(N, \beta)^2}. \quad (5)$$

195 In our analysis, we set $N = 2$ and $\beta = 1$ (C_2^1).

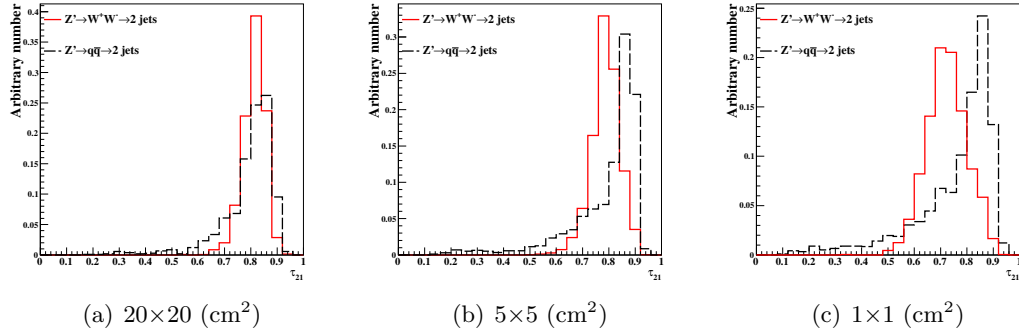


Figure 11: Distributions of τ_{21} in 20 TeV energy collision for different detector sizes. Cell sizes in 20×20 , 5×5 , and 1×1 cm^2 are shown here.

Figure 15 presents the histograms of C_2^1 with $\sqrt{s} = 20$ TeV after making requirement on the soft drop mass. The signal considered is $Z' \rightarrow WW$. Figure 16 shows the ROC curves from different detector cell sizes for each c.m. energy, respectively. One can see that the smallest detector cell size (1×1 cm^2) does not have the best signal/background separation power. Figure 17(c) summarizes the result of the Mann Whitney U test for C_2^1 . When c.m. energy increases, no improvement is observed from detector with the smallest cell size.

6. Conclusions

The studies presented in this paper show that the reconstruction of jet substructure variables for future particle colliders will benefit from small cell sizes of the hadronic calorimeters. This conclusion was obtained using the realistic Geant4 simulation of calorimeter responses combined with reconstruction of calorimeter clusters used as inputs for jet reconstruction. Hadronic calorimeters that use the cell sizes of 20×20 cm^2 are least performant almost for every substructure variables considered in this analysis for jet transverse momenta between 2.5 to 10 TeV. Such cell sizes are close to the nuclear interaction length of the considered calorimeter, and are similar to those used for the ATLAS and CMS detectors. The performance of hadronic calorimeters with 2×2 cm^2 and 1×1 cm^2 cells are found to be similar.

It is however interesting to note that, for very boosted jets with transverse momenta close to 20 TeV, no significant improvement with the decrease of cell sizes was observed. This result needs to be understood in terms of various type of simulations and different options for construction of the calorimeter clusters.

Acknowledgements

This research was performed using resources provided by the Open Science Grid, which is supported by the National Science Foundation and the U.S. Department of Energy's Office of Science. We gratefully acknowledge the computing resources provided

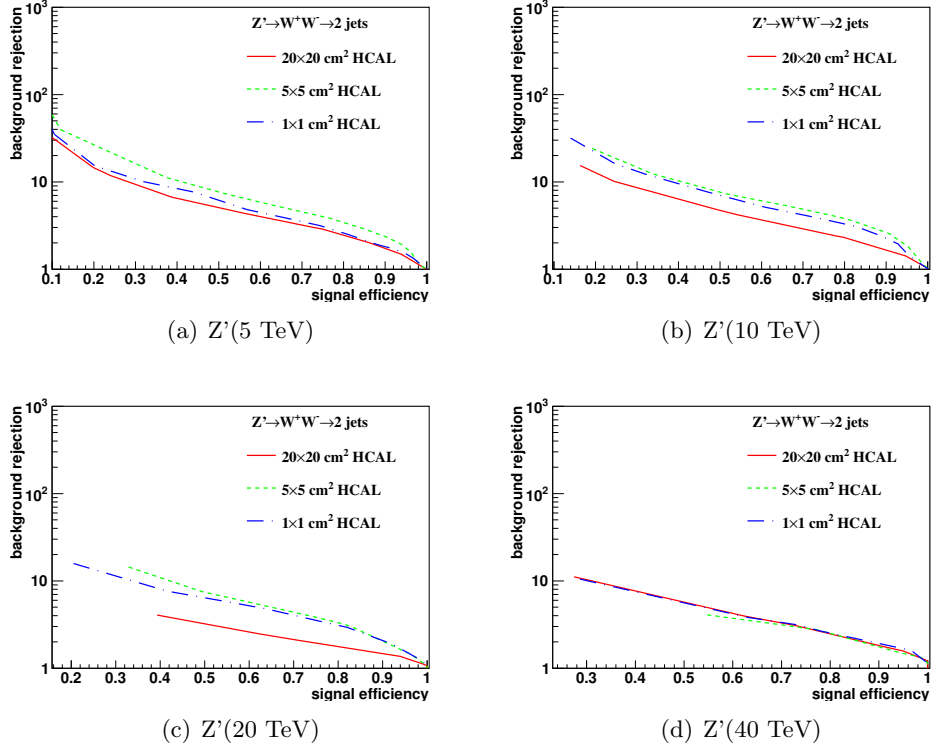


Figure 12: Signal efficiency versus background rejection rate using τ_{21} . The energies of collision at (a) 5, (b) 10, (c) 20, and (d) 40 TeV are shown here. In each figure, the three ROC curves correspond to different detector sizes.

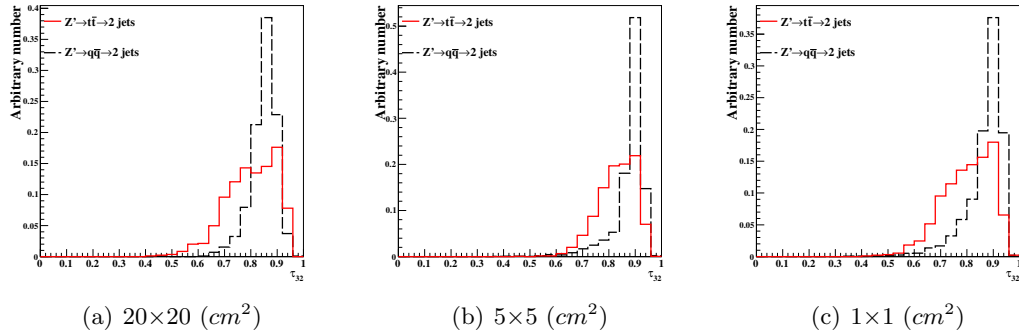


Figure 13: Distributions of τ_{32} in 20 TeV energy collision for different detector sizes. Cell sizes in 20×20 , 5×5 , and $1 \times 1 \text{ cm}^2$ are shown here.

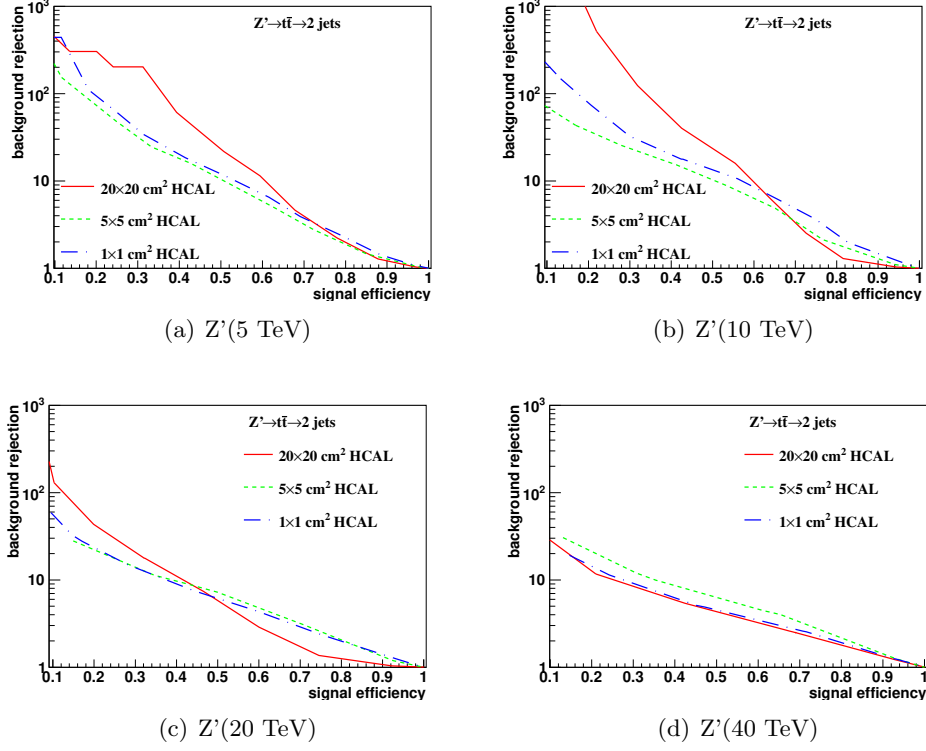


Figure 14: Signal efficiency versus background rejection rate using τ_{32} . The energies of collision at (a) 5, (b) 10, (c) 20, and (d) 40 TeV are shown here. In each figure, the three ROC curves correspond to different detector sizes.

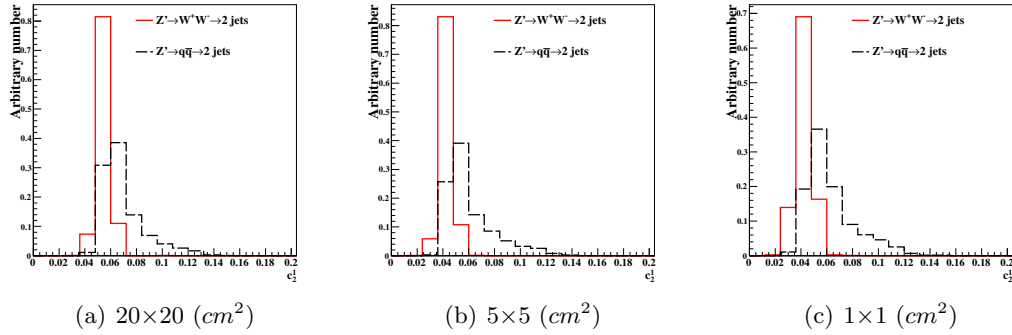


Figure 15: Distributions of C_2^1 in 20 TeV energy collision for different detector sizes. Cell sizes in 20×20 , 5×5 , and $1 \times 1 \text{ cm}^2$ are shown here.

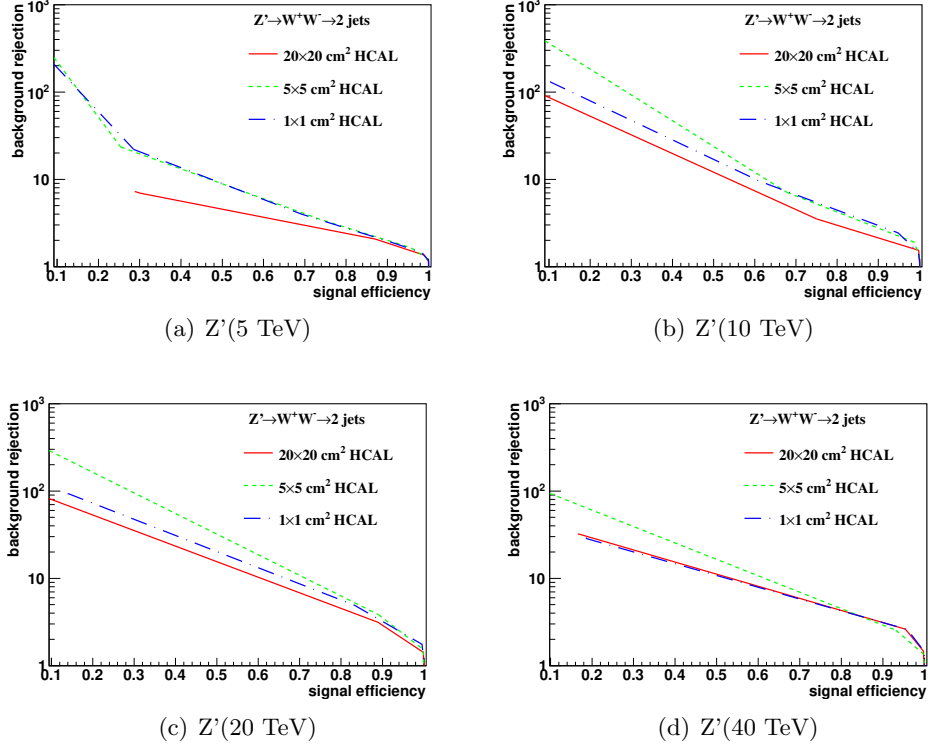


Figure 16: Signal efficiency versus background rejection rate using $C_2^{(1)}$. The energies of collision at (a) 5, (b) 10, (c) 20, and (d) 40 TeV are shown here. In each figure, the three ROC curves correspond to different detector sizes.

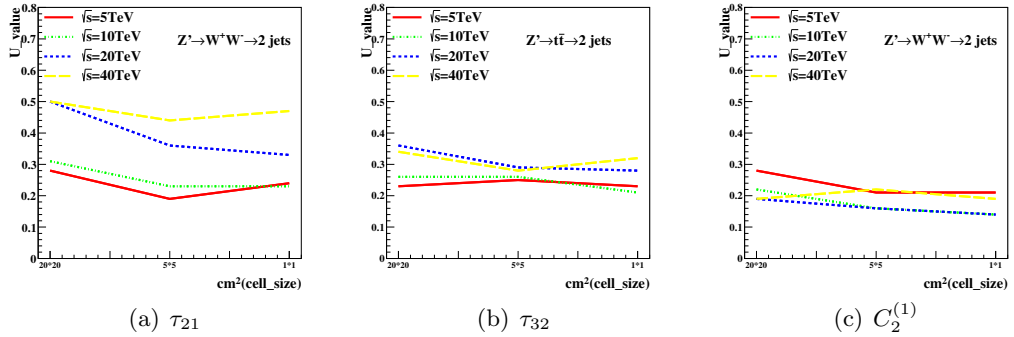


Figure 17: The Mann-Whitney U values for τ_{21} , τ_{32} , and $C_2^{(1)}$ reconstructed with different collision energies and detector cell sizes.

222 on Blues , a high-performance computing cluster operated by the Laboratory Comput-
223 ing Resource Center at Argonne National Laboratory. Argonne National Laboratory's
224 work was supported by the U.S. Department of Energy, Office of Science under con-
225 tract DE-AC02-06CH11357. The Fermi National Accelerator Laboratory (Fermilab) is
226 operated by Fermi Research Alliance, LLC under Contract No. DE-AC02-07CH11359
227 with the United States Department of Energy.

228 References

- 229 [1] M. Benedikt, [The Global Future Circular Colliders Effort](#) CERN-ACC-SLIDES-2016-0016. Pre-
230 sented at P5 Workshop on the Future of High Energy Physics, BNL, USA, Dec. 15-18, 2013.
231 URL <http://cds.cern.ch/record/2206376>
- 232 [2] J. Tang, et al., Concept for a Future Super Proton-Proton Collider (2015). [arXiv:1507.03224](#).
- 233 [3] R. Calkins, et al., [Reconstructing top quarks at the upgraded LHC and at future accelerators](#),
234 in: Proceedings, Community Summer Study 2013: Snowmass on the Mississippi (CSS2013): Min-
235 neapolis, MN, USA, July 29-August 6, 2013. [arXiv:1307.6908](#).
236 URL <https://inspirehep.net/record/1244676/files/arXiv:1307.6908.pdf>
- 237 [4] S. V. Chekanov, J. Dull, Energy range of hadronic calorimeter towers and cells for high-pT jets
238 at a 100 TeV collider [arXiv:1511.01468](#).
- 239 [5] E. Coleman, M. Freytsis, A. Hinzmann, M. Narain, J. Thaler, N. Tran, C. Vernieri, The importance
240 of calorimetry for highly-boosted jet substructure [arXiv:1709.08705](#).
- 241 [6] DELPHES 3 Collaboration, J. de Favereau, C. Delaere, P. Demin, A. Giammanco, V. Lematre,
242 A. Mertens, M. Selvaggi, DELPHES 3, A modular framework for fast simulation of a generic
243 collider experiment, JHEP 02 (2014) 057. [arXiv:1307.6346](#), [doi:10.1007/JHEP02\(2014\)057](#).
- 244 [7] S. V. Chekanov, M. Beydler, A. V. Kotwal, L. Gray, S. Sen, N. V. Tran, S. S. Yu, J. Zuzelski, Initial
245 performance studies of a general-purpose detector for multi-TeV physics at a 100 TeV pp collider,
246 JINST 12 (06) (2017) P06009. [arXiv:1612.07291](#), [doi:10.1088/1748-0221/12/06/P06009](#).
- 247 [8] J. Allison, et al., Recent developments in Geant4, Nuclear Instruments and Methods in Physics
248 Research A 835 (2016) 186.
- 249 [9] M. J. Charles, PFA Performance for SiD, in: Linear colliders. Proceedings, International Linear
250 Collider Workshop, LCWS08, and International Linear Collider Meeting, ILC08, Chicago, USA,
251 November 16-20, 2008 , 2009. [arXiv:0901.4670](#).
- 252 [10] J. S. Marshall, M. A. Thomson, Pandora Particle Flow Algorithm, in: Proceedings, International
253 Conference on Calorimetry for the High Energy Frontier (CHEF 2013), 2013, pp. 305–315. [arXiv:](#)
254 [1308.4537](#).
- 255 [11] G. P. S. M. Cacciari, G. Soyez, FastJet user manual CERN-PH-TH/2011-297. [arXiv:1111.6097](#).
- 256 [12] M. Cacciari, G. P. Salam, G. Soyez, The anti-kt jet clustering algorithm, JHEP 0804 (2008) 063.
257 [arXiv:0802.1189](#).
- 258 [13] S. Chekanov, HepSim: a repository with predictions for high-energy physics experiments, Advances
259 in High Energy Physics 2015 (2015) 136093, available as <http://atlaswww.hep.anl.gov/hepsim/>.
- 260 [14] B. Auerbach, S. Chekanov, J. Love, J. Proudfoot, A. Kotwal, Sensitivity to new high-mass states
261 decaying to $t\bar{t}b\bar{a}$ at a 100 TeV collider [arXiv:1412.5951](#).
- 262 [15] J. Butterworth, B. Cox, J. R. Forshaw, WW scattering at the CERN LHC, Phys.Rev. D65 (2002)
263 096014. [arXiv:hep-ph/0201098](#), [doi:10.1103/PhysRevD.65.096014](#).
- 264 [16] S. Catani, Y. L. Dokshitzer, M. H. Seymour, B. R. Webber, [Longitudinally-invariant k-clustering](#)
265 [algorithms for hadron-hadron collisions](#), Nuclear Physics B 406 (12) (1993) 187 – 224.
266 URL <http://www.sciencedirect.com/science/article/pii/055032139390166M>
- 267 [17] S. D. Ellis, D. E. Soper, Successive combination jet algorithm for hadron collisions, Phys. Rev.
268 D48 (1993) 3160–3166. [arXiv:hep-ph/9305266](#), [doi:10.1103/PhysRevD.48.3160](#).
- 269 [18] ATLAS Collaboration Collaboration, G. Aad, et al., Jet mass and substructure of inclusive jets in
270 $\sqrt{s} = 7$ TeV pp collisions with the ATLAS experiment, JHEP 1205 (2012) 128. [arXiv:1203.4606](#),
271 [doi:10.1007/JHEP05\(2012\)128](#).
- 272 [19] A. J. Larkoski, S. Marzani, G. Soyez, J. Thaler, Soft Drop, JHEP 05 (2014) 146. [arXiv:1402.2657](#),
273 [doi:10.1007/JHEP05\(2014\)146](#).
- 274 [20] Y. L. Dokshitzer, G. D. Leder, S. Moretti, B. R. Webber, Better jet clustering algorithms, JHEP
275 08 (1997) 001. [arXiv:hep-ph/9707323](#), [doi:10.1088/1126-6708/1997/08/001](#).
- 276 [21] M. Wobisch, T. Wengler, Hadronization corrections to jet cross-sections in deep inelastic scattering,
277 in: Monte Carlo generators for HERA physics. Proceedings, Workshop, Hamburg, Germany, 1998-
278 1999, 1998, pp. 270–279. [arXiv:hep-ph/9907280](#).
- 279 [22] J. Thaler, K. Van Tilburg, Identifying Boosted Objects with N-subjettiness, JHEP 03 (2011) 015.
280 [arXiv:1011.2268](#), [doi:10.1007/JHEP03\(2011\)015](#).
- 281 [23] S. Catani, Y. L. Dokshitzer, M. H. Seymour, B. R. Webber, Longitudinally-invariant k_{\perp} -clustering
282 algorithms for hadron-hadron collisions, Nucl. Phys. B 406 (CERN-TH-6775-93. LU-TP-93-2)
283 (1993) 187–224.

- 284 [24] F. A. Dreyer, L. Necib, G. Soyez, J. Thaler, Recursive Soft Drop, JHEP 06 (2018) 093. [arXiv:](#)
285 [1804.03657](#), [doi:10.1007/JHEP06\(2018\)093](#).
- 286 [25] A. J. Larkoski, G. P. Salam, J. Thaler, Energy Correlation Functions for Jet Substructure, JHEP
287 06 (2013) 108. [arXiv:1305.0007](#), [doi:10.1007/JHEP06\(2013\)108](#).